From Histology to *in vivo* MRI: An Implicit Neural Representation Framework for Medial Temporal Lobe Subregion Segmentation

Yue Li[1⋆](✉), Amanda E. Denning[1⋆], Zahra Khodakarami[1], Pulkit Khandelwal[2], Long Xie[1], Christopher A. Brown[1], Laura E. M. Wisse[3], Sandhitsu R. Das[1], David A. Wolk[1], and Paul A. Yushkevich[1]

[1] University of Pennsylvania, Philadelphia, USA
liyue3780@gmail.com (✉)
[2] Massachusetts General Hospital and Harvard Medical School, Boston, USA
[3] Lund University, Lund, Sweden

Abstract. Structural changes of subregions in the medial temporal lobe (MTL) reflect the progression of Alzheimer's disease. T2-weighted (T2w) MRI provides detailed depiction of the hippocampus and is the main *in vivo* modality for MTL subregion segmentation. However, the existing *in vivo* segmentation protocol relies on geometric rules rather than cytoarchitectonic criteria, which limits the anatomical accuracy of the resulting subregions. To address this, a cytoarchitecture-based protocol can be defined by mapping cytoarchitectonic annotations from histology to *in vivo* MRI. The main challenge of this mapping lies in the anisotropic resolution of T2w MRI, on which the continuous histology-defined boundaries become fragmented. In this work, we employ an implicit neural representation to construct a continuous *in vivo* representation of the MTL, onto which histology-defined boundaries are recovered smoothly. An isotropic segmentation method for fine-grained subregions is then developed with a coarse-to-fine two-stage framework. Compared with the anisotropic model trained in the original T2w space, the isotropic model achieves higher Dice scores in cross-validation. On the test set, the anisotropic model shows severe detection failures on fine-grained subregions, while the proposed model achieves the highest detection rate. Imaging biomarkers extracted from the proposed segmentation also achieve higher AUC values in early-affected AD subregions, in distinguishing amyloid-positive mild cognitive impairment from amyloid-negative cognitively unimpaired participants, compared to the other methods. This study shows that a continuous representation can effectively recover the anatomical structure of the MTL *in vivo*, lowering the barrier to using cytoarchitectonic boundaries for *in vivo* applications. Code is available.

Keywords: Histology · *in vivo* MRI · Implicit Neural Representation · Alzheimer's Disease.

[3] ⋆ These authors contributed equally.

1 Introduction

Imaging biomarkers of Alzheimer's disease (AD) extracted from structural MRI are widely used for diagnosis [17], disease monitoring [9,18], and as outcomes in clinical trials [3]. Recent studies showed that different subregions of the medial temporal lobe (MTL) have differential sensitivity to AD-related pathology [21,8], making accurate delineation of these subregions important for *in vivo* imaging in AD [6,5].

Conventional methods delineate MTL subregion boundaries based on geometrical rules and anatomical landmarks [20,1], which may not reflect the underlying cytoarchitecture. To bridge this gap, a recent study uses histology slides, postmortem MRI, and *in vivo* MRI to map histology-defined boundaries into *in vivo* image analysis [7]. With the cellular-level cytoarchitectural details in histology, the coarse subregions can be further divided into fine-grained subregions. For example, the entorhinal cortex (ERC) can be subdivided into eight fine-grained subregions, including entorhinal caudal (EC), entorhinal intermediate (EI), entorhinal lateral caudal (ELc), etc [7,19].

However, a spatial representation gap exists between the histology and *in vivo* MRI spaces. Boundaries in histology are defined on a nearly continuous 2D domain (pixel size $<1\mu$m), while the T2-weighted (T2w) *in vivo* MRI, preferred for MTL subregion segmentation, is acquired on an anisotropic, discretely sampled grid (voxel size $\sim 0.4\times0.4\times2.6\text{mm}^3$). Once transferred from histology to postmortem MRI and then to *in vivo* MRI, the continuous boundary becomes fragmented [7], losing fine details that automatic segmentation relies on. Super-resolution methods [4,14,22] may address this by upsampling T2w MRI to isotropic resolution, but they need paired low- and high-resolution images for training, and isotropic T2w (e.g., $\sim 0.4\times0.4\times0.4\text{mm}^3$) MRI is not available in practice, especially in older participants. Cross-modality super-resolution [12] can be trained without isotropic T2w images, but the domain gap between modalities limits its accuracy.

To address this mismatch, we employ a multi-modality implicit neural representation (INR) [15] to construct a continuous representation of the *in vivo* MTL, enabling cytoarchitectonic subregions to be defined in the isotropic *in vivo* space. Based on this representation, a two-stage segmentation framework is developed. It improves segmentation accuracy, increases the detection rate of fine-grained subregions, and extracts more effective imaging biomarkers.

2 Methods

2.1 Dataset

Training Set The training data were collected from 17 participants for whom antemortem (i.e., *in vivo*) T2w MRI ($\sim 0.4\times0.4\times2.6\text{mm}^3$), high-resolution postmortem MRI ($\sim 0.2\times0.2\times0.2\text{mm}^3$), and histology images of the MTL were all available. The mean age at death of the participants was 74.71 ± 7.09 years, including eight females and nine males.

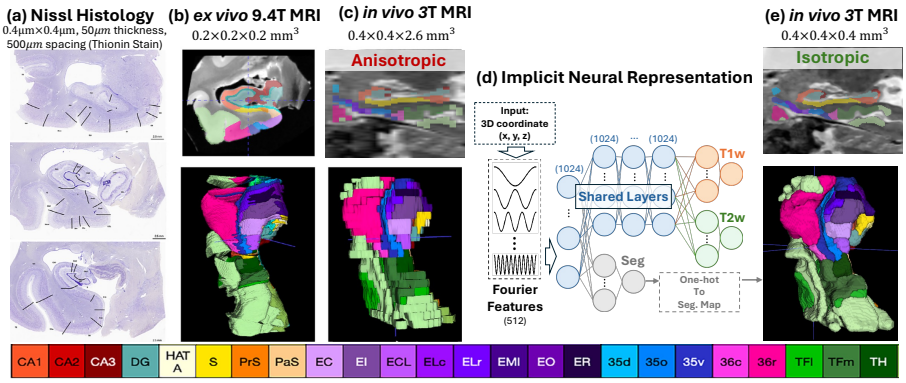

Fig. 1. Example of the multi-step process for defining cytoarchitectonic subregions in the isotropic *in vivo* space.

Subregions were manually segmented on the histology images by a team of neuroanatomists according to cytoarchitectural features (Fig. 1(a)), and then co-registered to the postmortem 9.4T MRI (Fig. 1(b)) [19]. To build the *in vivo* ground-truth segmentations, these segmentations were manually mapped to the *in vivo* 3T-T2w image space (Fig. 1(c)) using the *in vivo* T1w image as an intermediate registration reference [12]. The registered segmentations were manually edited to correct registration errors. The full list of cytoarchitectural labels, organized into coarse and fine-grained subregions, along with their full names and abbreviations, is shown in Table 1.

Test Set A cross-sectional test set of T2w *in vivo* MRI of 200 participants was selected from an *in vivo* cohort at the Penn AD Research Center (ADRC). The mean age at MRI scanning of the participants was 71.33 ± 5.82 years, including 129 females and 71 males. Based on the amyloid-PET scan closest in date to the MRI, the participants were classified as either amyloid-beta-negative cognitively unimpaired (A-CU, n=145) or amyloid-beta-positive with mild cognitive impairment (A+MCI, n=55). Both 3T anisotropic T2w and isotropic T1w images were available for each participant. This test set did not have manual segmentation as ground-truth so it was used to evaluate the model in downstream tasks.

2.2 Continuous Representation via INR

The T1w image has higher out-of-plane resolution (0.8 or 1 mm) and T2w image has higher in-plane resolution (0.4×0.4 mm^2). To make them contribute together to the continuous representation, a rigid transformation is estimated between the T1w and T2w images, and neither image is resampled into the space of the other in order to preserve their original voxel intensities as input to the INR model.

The INR model (Fig. 1(d)) is an incremental modification of the McGinnis et al. [15] model and consists of a coordinate feature extractor, a shared multi-layer

Table 1. Coarse subregions and histology-defined fine-grained subregions of the medial temporal lobe.

Coarse	**Fine-grained**
Hippocampus	Cornu Ammonis 1-3 (CA1-CA3), Hippocampal Amygdaloid Transitional Area (HATA)
Dentate Gyrus (DG)	Dentate Gyrus (DG)
Subiculum (SUB)	Parasubiculum (PaS), Presubiculum (PrS), Subiculum (S)
Entorhinal Cortex (ERC)	Entorhinal Caudal (EC), Entorhinal Intermediate (EI), Entorhinal Caudal Limiting (ECL), Entorhinal Lateral Caudal (ELc), Entorhinal Lateral Rostral (ELr), Entorhinal Medial Intermediate (EMI), Entorhinal Olfactory (Eo), Entorhinal Rostral (Er)
Brodmann Area 35 (BA35)	Brodmann Area 35 Dorsal (35d), Brodmann Area 35 Oblique (35o), Brodmann Area 35 Oblique Ventral (35v)
Brodmann Area 36 (BA36)	Brodmann Area 36 Caudal (36c), Brodmann Area 36 Rostral (36r)
Parahippocampal Cortex (PHC)	Area TF Lateral (TFl), Area TF Medial (TFm), Area TH (TH)

perceptron (MLP) backbone, and three reconstruction branches. The input consists of spatial coordinates from both the T1w and T2w spaces. Each coordinate is encoded into 512-dimensional Fourier features and processed by a four-layer shared MLP with a hidden dimension of 1024. The T1w and T2w branches are attached to the final shared layer, and the segmentation branch is attached after the first shared layer [11].

The T1w and T2w branches output the reconstructed images, supervised by the image intensity at each coordinate using mean squared error loss. Different from [15], we introduce an additional segmentation branch supervised by the manual segmentations. Specifically, the manual segmentations are converted into one-hot representations, and each channel of the segmentation branch output is optimized with cross-entropy loss [11]. After 60 training epochs, the learned representation is sampled on an isotropic grid of $0.4 \times 0.4 \times 0.4$ mm^3 to generate isotropic T1w, T2w, and segmentation maps (Fig. 1(e)).

2.3 Coarse-to-Fine Subregion Segmentation

A multi-modality subregion segmentation framework based on nnUNet [11,10] is used to segment the fine-grained subregions on *in vivo* T1w and T2w images. Given that the fine-grained subregions are nested within coarse subregions by definition, and that directly segmenting the small fine-grained subregions may lose important anatomical context and lead to under-segmentation, this study proposes a two-stage segmentation pipeline. The first stage segments the coarse subregions, and the second stage takes the segmented coarse subregions as prior information to perform the fine-grained segmentation. Specifically, once the first stage has segmented the coarse subregions, each coarse subregion is converted

into a binary map and added as an extra channel alongside the T1w and T2w images. The second stage therefore receives two intensity channels together with several coarse-subregion channels as its input.

The input to the segmentation model is a pair of T1w and T2w MRI images, where the T1w image is rigidly registered to the T2w image and both are linearly interpolated to an isotropic resolution of $0.4 \times 0.4 \times 0.4$ mm^3. The ground truth for training the segmentation model is the INR-generated isotropic manual segmentation (Fig. 1(e)) produced in the section 2.2. The model then produces the isotropic subregion segmentation. It should be noted that the INR-generated isotropic MRI is not used as input because training an INR is time-consuming (about half an hour per MTL), which is not acceptable during model inference.

2.4 Validation

Two baseline models are compared with the proposed model. The first is an nnUNet trained at the original (anisotropic) T2w resolution [13]. The second is an isotropic model that segments fine-grained subregions in a single stage [11]. Subregion 35d, present in only 8 out of 17 training cases, was excluded from evaluation. Three tasks are used to assess their performance.

1. The Dice score is computed by five-fold cross-validation on the training set.
2. The number of detection failures (i.e., subregions with no segmented voxel) is counted for each fine-grained subregion on the test set.
3. The hippocampal subregion volume and cortical subregion median thickness are calculated and used to distinguish A+MCI from A-CU participants in the test set. Area under the curve (AUC) is used to quantify the discrimination performance.

3 Results

3.1 Dice Score Evaluation

The average Dice score of each fine-grained subregion was computed through five-fold cross-validation on the training set, with results given in Table 2.

In the hippocampal subregions, smaller regions such as CA2 had lower Dice scores, consistent with previous studies [25,24]. In the cortical subregions, low Dice scores appeared even in larger regions such as 35v and TFl, likely reflecting the anatomical variability of cytoarchitectonic boundaries reported in [23].

The isotropic models achieved higher Dice scores than the anisotropic model, suggesting that learning from a continuous representation helped locate subregion boundaries more accurately. Comparing the two isotropic models, the proposed two-stage model had slightly lower Dice scores than the one-stage model, possibly because errors from both stages accumulated during inference. However, it still outperformed the anisotropic model, and its advantage became clearer in the downstream evaluations described below.

Table 2. Cross-validation mean Dice scores of each subregion on the training set. Higher is better. The best value is in **bold** and the second best is underlined. Vol.: mean volume of each subregion in the training set (mm^3). Aniso: anisotropic model; Iso-1: one-stage isotropic model; Iso-2: proposed two-stage isotropic model.

Subregion		Vol.	Aniso	Iso-1	Iso-2
Hippo	CA1	1094	0.715	**0.737**	0.734
	CA2	54	0.304	**0.318**	0.304
	CA3	271	0.559	**0.581**	0.556
	HATA	38	0.327	0.352	**0.404**
Sub	PaS	51	0.347	**0.404**	0.381
	PrS	169	0.540	**0.565**	0.557
	S	485	0.583	**0.624**	0.621
DG	DG	500	0.694	0.707	**0.718**
ERC	EC	94	0.402	**0.432**	0.398
	EI	158	0.608	**0.628**	0.594
	ECL	142	0.417	**0.454**	0.452
	ELc	48	0.371	**0.377**	0.281
ERC	ELr	133	0.388	**0.450**	0.433
	EMI	36	0.284	**0.415**	0.405
	Eo	59	0.359	**0.375**	0.368
	Er	64	0.428	**0.453**	0.412
BA35	35o	113	0.343	**0.374**	0.371
	35v	339	0.339	0.414	**0.424**
BA36	36c	248	0.286	**0.367**	0.337
	36r	496	0.470	**0.508**	0.506
PHC	TFl	399	0.253	**0.285**	0.279
	TFm	296	0.268	**0.270**	0.262
	TH	129	0.345	0.366	**0.381**

3.2 Detection Failure Evaluation

Given their small size, the fine-grained subregions are often missed during segmentation. We therefore counted the number of detection failures produced by each of the three segmentation methods, with the results given in Table 3. The anisotropic model missed more subregions than the other two methods, while the proposed two-stage model missed the fewest on the test set.

Fig. 2 shows two typical cases in which the anisotropic model failed to detect subregions in the anterior MTL. In both cases, the one-stage isotropic model produced more complete segmentations than the anisotropic model, and the proposed two-stage isotropic model further segmented additional subregions that were missed by the other two models.

3.3 Group Discrimination Evaluation

For each fine-grained subregion, we extracted the volume of hippocampal subfields and the median thickness of cortical MTL subregions. These measurements were then used to distinguish A+MCI from A-CU cases. A general linear model was fitted for each measurement. For hippocampal subregion volumes, age and intracranial volume were included as covariates. For cortical subregion median thickness, only age was included. The residuals were then used to compute the AUC. The resulting AUC values are given in Table 4.

The proposed two-stage isotropic model achieved the highest AUC in the largest number of subregions among the three methods, especially in the fine-grained subregions of the ERC, which is one of the earliest regions affected in AD [16,2]. The lower AUC of the anisotropic model may be explained by measurement inaccuracy in anisotropic space. Anisotropic voxels amplify segmentation

Table 3. Number of detection failures of each subregion across 200 test subjects under different models. Lower is better. The best value is in **bold** and the second best is underlined. Aniso: anisotropic model; Iso-1: one-stage isotropic model; Iso-2: proposed two-stage isotropic model.

Subregion		Aniso	Iso-1	Iso-2
Hippo	CA1	**0**	**0**	**0**
	CA2	1	**0**	**0**
	CA3	**0**	**0**	**0**
	HATA	87	**9**	11
Sub	PaS	**0**	**0**	**0**
	PrS	**0**	**0**	**0**
	S	**0**	**0**	**0**
DG	DG	**0**	**0**	**0**
ERC	EC	2	3	**0**
	EI	9	9	**0**
	ECL	2	**0**	**0**
	ELc	49	22	**5**
ERC	ELr	31	25	**8**
	EMI	122	18	**6**
	Eo	70	31	**12**
	Er	62	26	**11**
BA35	35o	11	4	**0**
	35v	4	1	**0**
BA36	36c	18	**0**	**0**
	36r	20	14	**0**
PHC	TFl	5	**0**	**0**
	TFm	1	**0**	**0**
	TH	1	**0**	**0**

errors in volume estimation, and stair-like surfaces along the low-resolution direction bias thickness measurement. The proposed isotropic segmentation reduced these effects.

4 Discussion and Conclusion

The benefit of the proposed framework can be explained from 3D continuity. For fine-grained subregions that span a small number of voxels within a coronal slice, morphological features degrade into noise, leaving only local intensity contrast as a cue. Inter-slice continuity then becomes important, but the anisotropic resolution prevents it from being exploited. By constructing a continuous representation, cytoarchitectonic boundaries can be defined continuously, enabling stable segmentation of fine-grained subregions.

Another strength of isotropic segmentation is that the convolutional kernel in the segmentation model is isotropic. When such a kernel is applied to an anisotropic image, the tissue appears compressed and does not match its true anatomical shape. Learning from this distorted structure can degrade the segmentation accuracy, particularly along the low-resolution direction.

Among the isotropic models, the proposed two-stage model produced fewer failed subregion detections and achieved higher AUC values in more subregions than the one-stage model. A likely strength of the two-stage model comes from its design. It first segments the coarse subregions, and then segments the fine-grained subregions using the coarse result as guidance. This coarse segmentation gives the second stage a broader reference context for locating the fine subregions. The one-stage model, in contrast, segments the fine-grained subregions directly. Because these subregions are small, only a limited neighborhood is available as

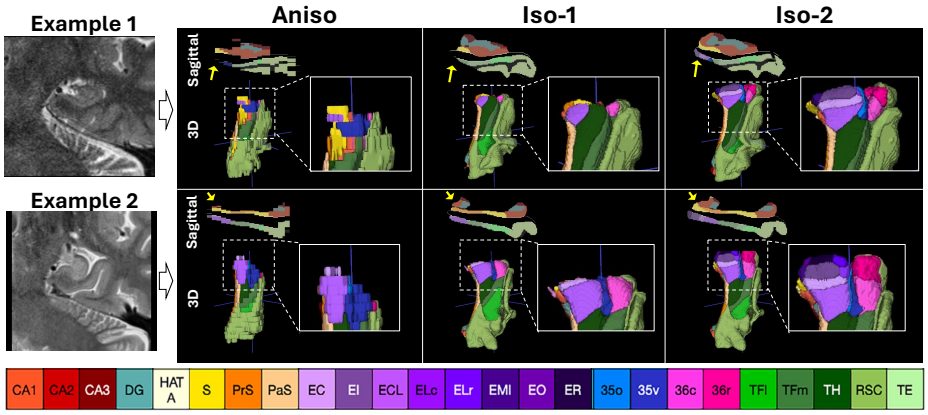

Fig. 2. Two examples of detection failures in the anterior MTL. The anisotropic model missed several subregions (yellow arrows and zoomed-in 3D views), the one-stage isotropic model partially recovered them, and the proposed two-stage isotropic model produced accurate segmentations at these locations. Aniso: anisotropic model; Iso-1: one-stage isotropic model; Iso-2: proposed two-stage isotropic model.

a reference. This is most severe in the anterior region, where no hippocampal structure is available as a reference, and there the one-stage model failed to detect some of the fine-grained ERC subregions.

A limitation of this study is that the input images to the segmentation model are not upsampled by the INR, a trade-off for inference efficiency since INR training is time-consuming and case-specific. Although the segmentation model produces smooth surfaces with this approach, some fine-grained tissue features may be lost.

In future work, we will develop a fast and generalizable INR that can be applied at inference time, allowing the input images and the segmentation to benefit from the continuous representation. Besides this, we will explore whether a continuous representation at an isotropic resolution higher than 0.4mm^3 provides further benefits, and whether signed distance transform interpolation can produce smoother label upsampling.

In conclusion, this study proposes a multi-modality INR framework that constructs a continuous representation of the MTL from T1w, T2w, and manual segmentations. The isotropic *in vivo* space provided by this representation allows cytoarchitecture-based fine-grained subregions to be continuously defined, facilitating the extraction of imaging biomarkers for AD.

Acknowledgments. This work was supported by NIH (grant numbers R01-AG069474, RF1-AG056014, P30-AG072979, R01-AG070592). LW is supported by MultiPark, a strategic research area at Lund University, and project grants from the Bente Rexed Gerstedt Foundation, Fondation Recherche Alzheimer and the Crafoord Foundation (20230790).

Table 4. AUC values of hippocampal subregion volume and cortical subregion median thickness in distinguishing A-CU from A+MCI, computed using a general linear model. The best value is in **bold** and the second best is underlined. Aniso: anisotropic model; Iso-1: one-stage isotropic model; Iso-2: proposed two-stage isotropic model.

	Subregion		Aniso	Iso-1	Iso-2	Subregion		Aniso	Iso-1	Iso-2
Left Side	Hippo	CA1	0.818	0.855	**0.861**	ERC	ELr	0.641	0.665	**0.674**
		CA2	0.633	0.668	**0.778**		EMI	0.565	0.656	**0.671**
		CA3	**0.603**	0.584	0.490		Eo	0.504	0.597	**0.663**
		HATA	**0.539**	0.523	0.468		Er	0.550	0.621	**0.661**
	Sub	PaS	0.562	0.619	**0.667**	BA35	35o	**0.707**	0.670	0.685
		PrS	0.634	**0.702**	0.687		35v	0.617	0.638	**0.660**
		S	0.694	0.765	**0.793**	BA36	36c	0.572	**0.670**	0.639
	DG	DG	0.604	0.686	**0.709**		36r	0.632	0.641	**0.644**
	ERC	EC	**0.745**	0.727	0.733	PHC	TFl	0.471	0.506	**0.523**
		EI	0.686	0.692	**0.723**		TFm	**0.574**	0.548	0.558
		ECL	0.740	**0.759**	0.694		TH	**0.651**	0.606	0.587
		ELc	0.697	**0.718**	0.701					
Right Side	Hippo	CA1	0.762	0.807	**0.825**	ERC	ELr	0.549	0.640	**0.650**
		CA2	0.667	0.653	**0.735**		EMI	0.468	**0.668**	0.647
		CA3	0.606	**0.616**	0.550		Eo	0.451	0.574	**0.637**
		HATA	0.437	**0.479**	0.427		Er	0.487	0.604	**0.638**
	Sub	PaS	0.633	0.623	**0.644**	BA35	35o	**0.638**	0.604	0.633
		PrS	0.643	0.663	**0.677**		35v	0.584	0.633	**0.665**
		S	0.665	0.747	**0.759**	BA36	36c	**0.597**	0.528	0.535
	DG	DG	0.555	**0.685**	0.678		36r	0.613	0.621	**0.636**
	ERC	EC	0.667	0.666	**0.677**	PHC	TFl	0.475	**0.556**	0.548
		EI	0.664	0.666	**0.726**		TFm	**0.633**	0.487	0.569
		ECL	0.655	**0.679**	0.636		TH	**0.640**	0.515	0.509
		ELc	0.600	0.698	**0.717**					

Disclosure of Interests. D.A.W. has served as a paid consultant to Eli Lilly and Beckman Coulter. He serves on a DSMB for GSK. He received grants from Biogen paid to his University. S.R.D. received consultation fees from Rancho Biosciences and Nia Therapeutics. Other authors have no conflict of interest to declare.

References

1. Berron, D., Vieweg, P., Hochkeppler, A., Pluta, J., Ding, S.L., Maass, A., Luther, A., Xie, L., Das, S., Wolk, D., et al.: A protocol for manual segmentation of medial temporal lobe subregions in 7 tesla mri. NeuroImage: Clinical **15**, 466–482 (2017)
2. Braak, H., Braak, E.: Neuropathological stageing of alzheimer-related changes. Acta neuropathologica **82**(4), 239–259 (1991)
3. Cash, D.M., Rohrer, J.D., Ryan, N.S., Ourselin, S., Fox, N.C.: Imaging endpoints for clinical trials in alzheimer's disease. Alzheimer's research & therapy **6**(9), 87 (2014)
4. Chen, Y., Shi, F., Christodoulou, A.G., Xie, Y., Zhou, Z., Li, D.: Efficient and accurate mri super-resolution using a generative adversarial network and 3d multi-

level densely connected network. In: International conference on medical image computing and computer-assisted intervention. pp. 91–99. Springer (2018)
5. Daugherty, A.M., Carr, V., Canada, K.L., Rådman, G., Brown, T., Augustinack, J., Amunts, K., Bakker, A., Berron, D., Burggren, A., et al.: Harmonized protocol for subfield segmentation in the hippocampal body on high-resolution in vivo mri from the hippocampal subfields group (hsg). Hippocampus **36**(2), e70073 (2026)
6. DeKraker, J., Haast, R.A., Yousif, M.D., Karat, B., Lau, J.C., Köhler, S., Khan, A.R.: Automated hippocampal unfolding for morphometry and subfield segmentation with hippunfold. elife **11**, e77945 (2022)
7. Denning, A.E., Lim, S.A., Li, Y., Sadeghpour, N., Ravikumar, S., Ittyerah, R., Chung, E., Bedard, M., Prabhakaran, K., Trotman, W., et al.: Mapping anatomical boundaries from histology to antemortem mri to inform automatic segmentation of medial temporal lobe subregions. Alzheimer's & Dementia **20**, e091831 (2024)
8. de Flores, R., Wisse, L.E., Das, S.R., Xie, L., McMillan, C.T., Trojanowski, J.Q., Robinson, J.L., Grossman, M., Lee, E., Irwin, D.J., et al.: Contribution of mixed pathology to medial temporal lobe atrophy in alzheimer's disease. Alzheimer's & Dementia **16**(6), 843–852 (2020)
9. Gordon, B.A., Blazey, T.M., Su, Y., Hari-Raj, A., Dincer, A., Flores, S., Christensen, J., McDade, E., Wang, G., Xiong, C., et al.: Spatial patterns of neuroimaging biomarker change in individuals from families with autosomal dominant alzheimer's disease: a longitudinal study. The Lancet Neurology **17**(3), 241–250 (2018)
10. Isensee, F., Jaeger, P.F., Kohl, S.A., Petersen, J., Maier-Hein, K.H.: nnu-net: a self-configuring method for deep learning-based biomedical image segmentation. Nature methods **18**(2), 203–211 (2021)
11. Li, Y., Khandelwal, P., Jena, R., Xie, L., Duong, M., Denning, A.E., Brown, C.A., Wisse, L.E., Das, S.R., Wolk, D.A., et al.: Achieving detailed medial temporal lobe segmentation with upsampled isotropic training from implicit neural representation. arXiv preprint arXiv:2508.17171 (2025)
12. Li, Y., Khandelwal, P., Xie, L., Wisse, L.E., Denning, A.E., Brown, C.A., McGrew, E., Lim, S.A., Sadeghpour, N., Ravikumar, S., et al.: Imaging biomarkers for neurodegenerative diseases from detailed segmentation of medial temporal lobe subregions on in vivo brain mri using upsampling strategy guided by high-resolution ex vivo mri. arXiv preprint arXiv:2504.18442 (2025)
13. Li, Y., Xie, L., Khandelwal, P., Wisse, L.E., Brown, C.A., Prabhakaran, K., Tisdall, M.D., Mechanic-Hamilton, D., Detre, J.A., Das, S.R., et al.: Automatic segmentation of medial temporal lobe subregions in multi-scanner, multi-modality magnetic resonance imaging of variable quality. Hippocampus **35**(6), e70036 (2025)
14. Liang, J., Cao, J., Sun, G., Zhang, K., Van Gool, L., Timofte, R.: Swinir: Image restoration using swin transformer. In: Proceedings of the IEEE/CVF international conference on computer vision. pp. 1833–1844 (2021)
15. McGinnis, J., Shit, S., Li, H.B., Sideri-Lampretsa, V., Graf, R., Dannecker, M., Pan, J., Stolt-Ansó, N., Mühlau, M., Kirschke, J.S., et al.: Single-subject multi-contrast mri super-resolution via implicit neural representations. In: International Conference on Medical Image Computing and Computer-Assisted Intervention. pp. 173–183. Springer (2023)
16. Nelson, P.T., Alafuzoff, I., Bigio, E.H., Bouras, C., Braak, H., Cairns, N.J., Castellani, R.J., Crain, B.J., Davies, P., Tredici, K.D., et al.: Correlation of alzheimer disease neuropathologic changes with cognitive status: a review of the literature. Journal of Neuropathology & Experimental Neurology **71**(5), 362–381 (2012)

17. Olsen, R.K., Yeung, L.K., Noly-Gandon, A., D'Angelo, M.C., Kacollja, A., Smith, V.M., Ryan, J.D., Barense, M.D.: Human anterolateral entorhinal cortex volumes are associated with cognitive decline in aging prior to clinical diagnosis. Neurobiology of aging **57**, 195–205 (2017)
18. Phillips, J.S., Da Re, F., Irwin, D.J., McMillan, C.T., Vaishnavi, S.N., Xie, S.X., Lee, E.B., Cook, P.A., Gee, J.C., Shaw, L.M., et al.: Longitudinal progression of grey matter atrophy in non-amnestic alzheimer's disease. Brain **142**(6), 1701–1722 (2019)
19. Ravikumar, S., Denning, A.E., Lim, S., Chung, E., Sadeghpour, N., Ittyerah, R., Wisse, L.E., Das, S.R., Xie, L., Robinson, J.L., et al.: Postmortem imaging reveals patterns of medial temporal lobe vulnerability to tau pathology in alzheimer's disease. Nature communications **15**(1), 4803 (2024)
20. Sadeghpour, N., Lim, S.A., Wuestefeld, A., Denning, A.E., Ittyerah, R., Trotman, W., Chung, E., Sadaghiani, S., Prabhakaran, K., Bedard, M.L., et al.: Developing an anatomically valid segmentation protocol for anterior regions of the medial temporal lobe for neurodegenerative diseases. Hippocampus **35**(5), e70027 (2025)
21. Uchida, Y., Nishimaki, K., Kan, H., Iyatomi, H., Oishi, K.: Hippocampal subregional texture features associated with alzheimer's disease severity and cognition. Brain Communications **8**(3), fcag164 (2026)
22. Wang, J., Levman, J., Pinaya, W.H.L., Tudosiu, P.D., Cardoso, M.J., Marinescu, R.: Inversesr: 3d brain mri super-resolution using a latent diffusion model. In: International conference on medical image computing and computer-assisted intervention. pp. 438–447. Springer (2023)
23. Wuestefeld, A., Baumeister, H., Adams, J.N., de Flores, R., Hodgetts, C.J., Mazloum-Farzaghi, N., Olsen, R.K., Puliyadi, V., Tran, T.T., Bakker, A., et al.: Comparison of histological delineations of medial temporal lobe cortices by four independent neuroanatomy laboratories. Hippocampus **34**(5), 241–260 (2024)
24. Xie, L., Wisse, L.E., Wang, J., Ravikumar, S., Khandelwal, P., Glenn, T., Luther, A., Lim, S., Wolk, D.A., Yushkevich, P.A.: Deep label fusion: A generalizable hybrid multi-atlas and deep convolutional neural network for medical image segmentation. Medical image analysis **83**, 102683 (2023)
25. Yushkevich, P.A., Pluta, J.B., Wang, H., Xie, L., Ding, S.L., Gertje, E.C., Mancuso, L., Kliot, D., Das, S.R., Wolk, D.A.: Automated volumetry and regional thickness analysis of hippocampal subfields and medial temporal cortical structures in mild cognitive impairment. Human brain mapping **36**(1), 258–287 (2015)